< Letter >

Simultaneous Operando Time-Resolved XAFS–XRD Measurements of a Pt/C Cathode Catalyst in Polymer Electrolyte Fuel Cell under Transient Potential Operations

Oki Sekizawa,[†] *Tomoya Uruga,*[†,§] *Kotaro Higashi,*[†] *Takuma Kaneko,*[†] *Yusuke Yoshida,*[†] *Tomohiro Sakata,*[†] *and Yasuhiro Iwasawa*[†]*

[†] Innovation Research Center for Fuel Cells, The University of Electro-Communications, Chofugaoka, Chofu, Tokyo 182-8585, Japan

[§] Japan Synchrotron Radiation Research Institute, SPring-8, Sayo, Hyogo 679-5198, Japan

KEYWORDS. Simultaneous *operando* time-resolved QXAFS–XRD measurements; Pt/C cathode catalyst; polymer electrolyte fuel cell (PEFC); Transient response structural and electronic transformations.

Corresponding Author * Yasuhiro Iwasawa

E-mail: iwasawa@pc.uec.ac.jp

ABSTRACT. We have succeeded in simultaneous *operando* time-resolved QXAFS–XRD measurements at each acquisition time of 20 ms for a Pt/C cathode catalyst in PEFC, while measuring the current/charge of the PEFC during the transient voltage cyclic processes (0.4 V_{RHE} → 1.4 V_{RHE} → 0.4 V_{RHE}) under H_2(anode)–N_2(cathode). The rate constants for Pt-O bond formation/dissociation, Pt charging/discharging, Pt-Pt bond dissociation/reformation, and decrease/increase of Pt metallic-phase core size under the transient potential operations were determined by the combined time-resolved QXAFS–XRD technique. The present study provides a new insight into the transient-response reaction mechanism and structural transformation in the Pt surface layer and bulk, which are relevant to the origin of PEFC activity and durability as key issues for the development of next-generation PEFCs.

Introduction

Polymer electrolyte fuel cell (PEFC) can bring zero emission vehicles into reality in the future due to high power density and efficiency at low temperatures as launched recently by TOYOTA and HONDA, in which carbon-supported Pt-based nanoparticle catalysts (Pt/C) are used as cathode in membrane electrode assembly (MEA) of PEFC. Nevertheless, further improvements of the oxygen reduction reaction (ORR) activity and durability of cathode catalysts to remarkably reduce the Pt amount and PEFC stacking cost are indispensable.[1-10] To develop next-generation PEFCs for automobiles, the structural kinetics and dynamic behaviors of cathode catalysts relevant to molecular-level performances of MEAs under the harsh PEFC operating conditions must be understood more thoroughly. ORR performances and catalyst characterizations using soft-x ray XPS, TEM/SEM, XRD, NMR, FT-IR/ATR-IR, Raman, neutron scattering, etc. have extensively been studied to understand the PEFC catalysis. However, it is difficult to observe the dynamic behavior and transformation of Pt nanoparticles in MEAs with a stacking structure because there are few suitable *in situ* analysis methods to elucidate the transient response structural transformation and kinetics of Pt nanoparticle surfaces of Pt/C cathode inside MEA in PEFC.

Time-resolved quick X-ray absorption fine structure (QXAFS) enables *in situ* element-selective investigation on the dynamic transformations of *the local structures and oxidation states* of Pt nanoparticles in Pt/C cathode catalysts under the PEFC operating conditions,[12-17] while time-resolved X-ray diffraction (XRD) enables *in situ* measurements of dynamic transformations of *the long-period ordered crystalline structures* of Pt electrocatalysts.[18-20] We have designed a combined system for simultaneous time-resolved measurements of QXAFS and XRD of MEA cathode catalysts. Here we report the first example of simultaneous *operando* time-resolved QXAFS–XRD measurements at each acquisition time of 20 ms to evidence the dynamic structural and electronic behavior of an MEA Pt/C cathode catalyst under the transient voltage cyclic operations 0.4 V →1.4 V →0.4 V (vs RHE).

Experimental

The experiments and data analysis are described in supporting information (SI) in detail, but briefly described below. A cathode catalyst was Pt/C (Pt 46.1 wt%, TEC10E50E, Tanaka Kikinzoku Kogyo), and Ru/C (Ru 30 wt%, TECRu(ONLY)E50, Tanaka Kikinzoku Kogyo) was used as an anode catalyst to avoid interference against XAFS measurements of the Pt/C cathode. The MEA (3.0 × 3.3 cm, 0.6 mg-Pt/Ru cm^{-2}, Pt: 2.6 ± 0.9 nm) used in this study was provided by Eiwa Co. Ltd., Japan.

QXANES and QEXAFS spectra were analyzed in the similar way to the previous reports,[11,14,15] using the Larch code (v0.9.20a) containing the IFEFFIT Package (Athena and Artemis) (SI). The extracted k^3-weighted Pt L_{III}-edge EXAFS oscillations were Fourier transformed into R-space over k = 30–130 nm^{-1}, and the curve fittings were performed in the R-space (0.12–0.31 nm). XRD (111) and (220) diffraction peaks were fitted by the Gaussian function and Pt particle sizes in MEA Pt/C cathode catalysts were calculated by the Scherrer equation as described in SI. The rate constants for surface chemical reaction processes and Pt metallic-phase size change under the transient potential operations 0.4 V_{RHE} →1.4 V_{RHE} →0.4 V_{RHE} were determined from the time profiles of the QXAFS and XRD analysis data (SI).

Results and Discussion

Simultaneous time-resolved QXAFS–XRD measurement system for dynamic Pt/C cathode catalysts under PEFC operations.

The simultaneous *operando* time-resolved QXAFS–XRD measurements for MEA Pt/C under transient potential operations (anode: H_2; cathode: N_2) at 60 ms time-resolution (20 ms QXAFS x2 + 20 ms XRD x1 = 60 ms) were performed at SPring-8 BL36XU beamline, where the incident X-rays were irradiated to an MEA Pt/C cathode catalyst in a new *in situ* PEFC cell at an angle of

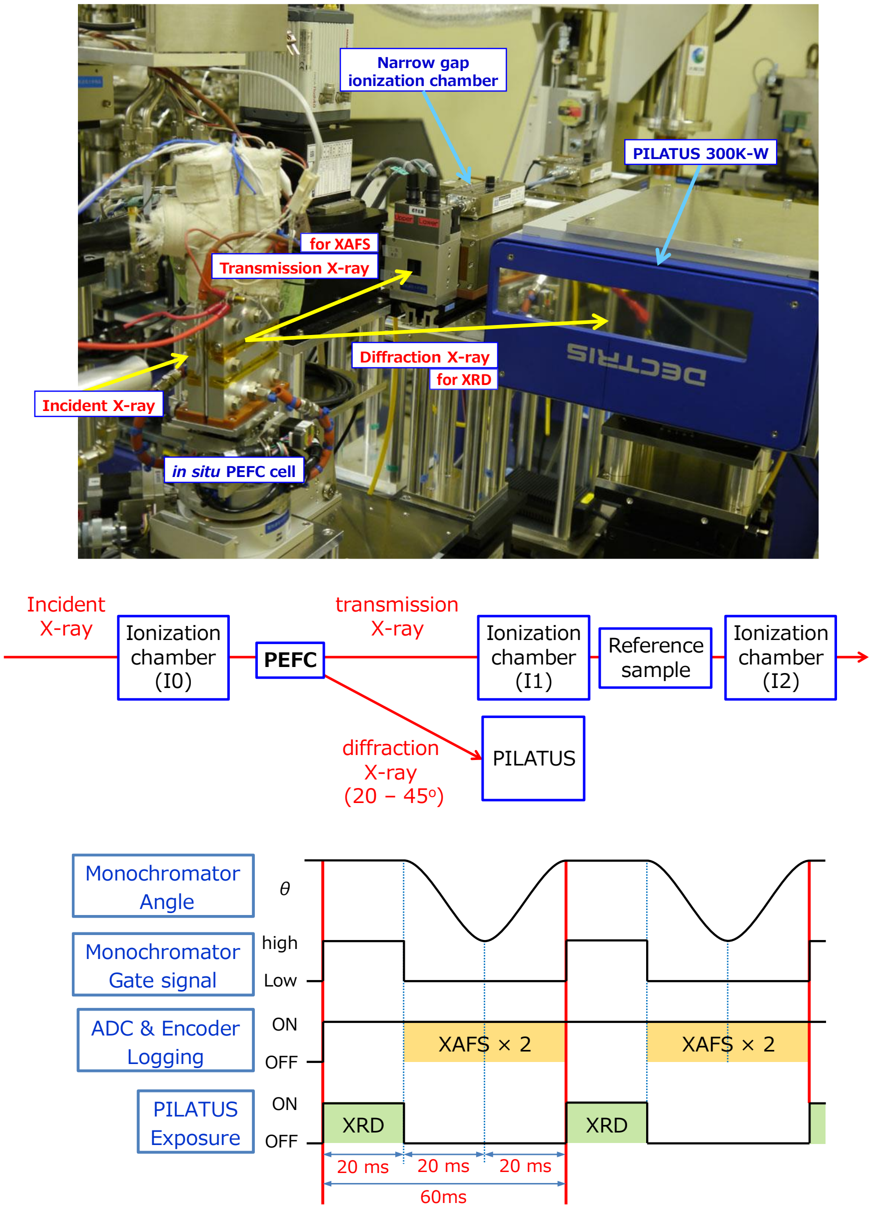

Figure 1. Experimental setup for *in situ* time-resolved XAFS and XRD measurements of PEFC Pt/C cathode catalysts under voltage operating conditions, a schematic diagram of the setup, a high-speed regulation pattern of monochromator angles with gate signals, and recording time charts of detectors for the simultaneous XAFS and XRD measurements

10^o to the MEA plane. The experimental setup for the simultaneous *operando* time-resolved measurements of QXAFS and XRD, while measuring the current/charge of PEFC during the potential operating processes, is shown in Figure 1, where a high-speed regulation pattern of monochromator angles for the simultaneous QXAFS–XRD measurements is also shown. The cell voltage was changed from the open-circuit voltage (OCV) to 0.4 V_{RHE}, where the voltage was kept for 300 s, followed by the rapid voltage jump from 0.4 V_{RHE} to1.4 V_{RHE}, and this voltage was kept for 300 s, and then reversely the cell voltage was jumped rapidly from 1.4 V_{RHE} to 0.4 V_{RHE}.

Transient response profiles of Pt nanoparticles in MEA Pt/C under voltage cyclic operations.

We have succeeded in measuring *operando* time-resolved Pt L_{III}-edge QXAFS spectra and XRD patterns for an MEA Pt/C at 60 ms time resolution by the developed combined technique using the new 10^o-incidence X-ray irradiation cell (Figure 1), while measuring the current/charge of the PEFC during the potential operating processes (0.4 V_{RHE} → 1.4 V_{RHE} → 0.4 V_{RHE}) under H_2(anode)–N_2(cathode). The typical QXAFS spectra, their oscillations and Fourier transforms at 0.4 V_{RHE} and 1.4 V_{RHE} are shown in Figure S1. The structural parameters determined by the curve-fitting QEXAFS analysis are listed in Table S1. The Pt metallic nanoparticles with 2.6 ± 0.9 nm dimension are regarded to constitute approximately 5 Pt layers, assuming sphere structures with the fcc arrangement.[14] At 1.4 V_{RHE} the CN(Pt-Pt) and CN(Pt-O) were determined to be 5.3 ±1.0 and 2.2 ± 0.5, respectively (Table S1), which are well reproduced by the values 5.7 (eq.(S2)) and 2.4 (eq.(S3)), respectively simulated by assuming the formation of a surface tetragonal $Pt^{2+}O$ phase layer.[11,14] The potential dependent surface structures at 0.4 V_{RHE} and 1.4 V_{RHE} are illustrated in Figure S2 (a) and (b), respectively.

We have successfully measured the transient response series of *operando* time-resolved QXAFS–XRD for a Pt/C cathode catalyst in PEFC under the voltage cyclic processes 0.4 V_{RHE}→ 1.4 V_{RHE}→0.4 V_{RHE} for the first time. The series of time-resolved QXANES spectra, QEXAFS Fourier transforms and XRD patterns of an MEA Pt/C in the transient potential operations are shown in Figure 2. The transient response time profiles of the QXANES white line peak height (proportional to Pt valence), CN(Pt-Pt) and CN(Pt-O) are plotted against the reaction time in Figure 2 (A), (B) and (C), respectively. The transient response time profiles of the XRD (220) peak

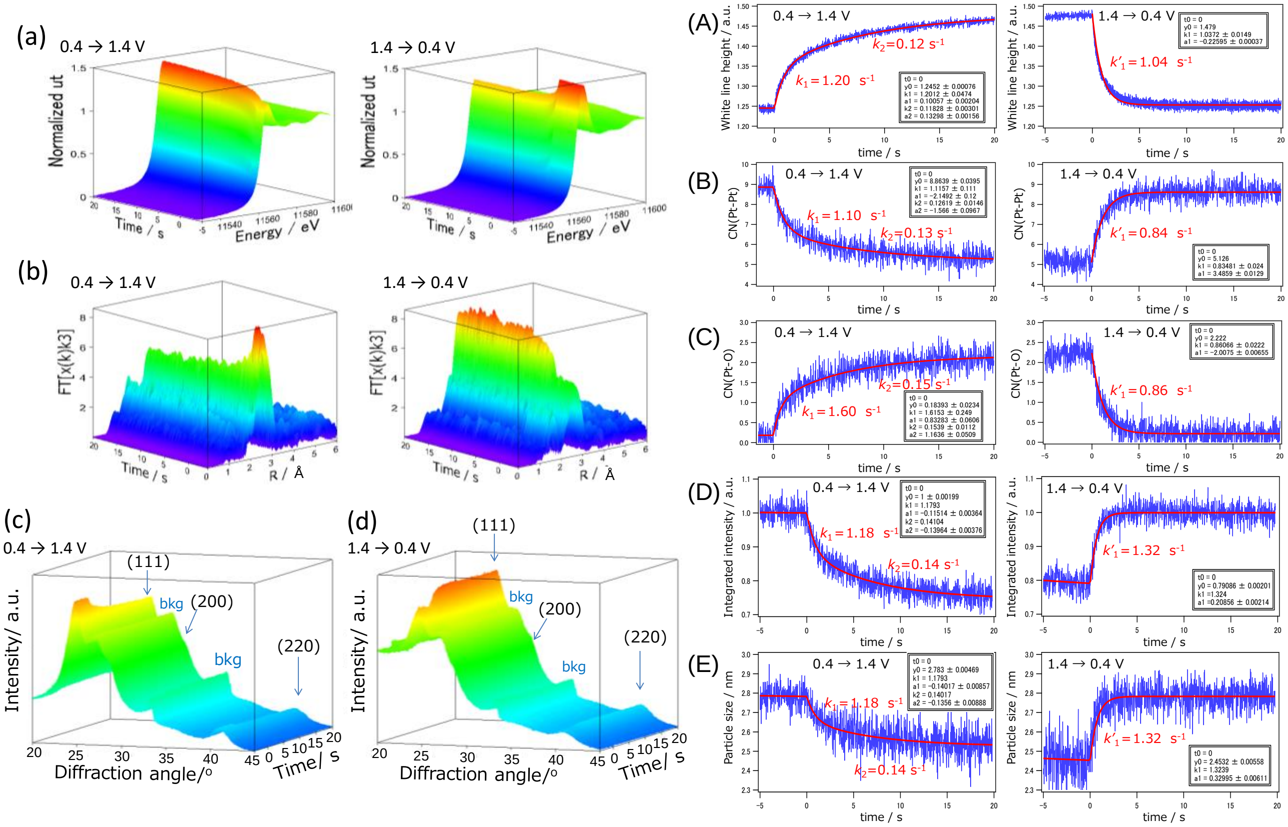

Figure 2. (left) The simultaneous time-resolved QXAFS–XRD measurements. The series of in situ time-resolved (a) QXANES spectra, (b) QEXAFS Fourier transforms and (c, d) XRD of Pt/C in PEFC in the transient potential operating processes 0.4 V_{RHE}→1.4 V_{RHE}→0.4 V_{RHE}. (c) and (d): time-resolved XRD patterns before subtraction of background (bkg) peaks.
(right) Transient response curves of the white line peak height (A), CN(Pt-Pt) (B), CN(Pt-O) (C), integrated (220) peak intensity (D) and Pt nanoparticle size (E) of the MEA Pt/C catalyst in the potential operations (0.4 V_{RHE}→1.4 V_{RHE}→0.4 V_{RHE}) under H_2(anode)–N_2(cathode); Cell temp.: 353 K; Relative humidity: ~93%. Time resolution: 20 ms.

integrated intensity and Pt metallic-nanoparticle sizes estimated by the Scherrer's formula are also shown in Figure 2 (D) and (E), respectively. A typical XRD pattern for the Pt/C cathode catalyst in MEA recorded by operando time-resolved XRD (acquisition time: 20 ms) is shown in Figure S3. The transient responses of the white line peak height, CN(Pt-Pt), CN(Pt-O), XRD (220) intensity and Pt metallic-phase size against the voltage cyclic operations 0.4 V_{RHE}→1.4 V_{RHE}→0.4 V_{RHE} were analyzed by the following one or two exponential functions, $f(t) = y_0 + a_1 \exp(-k_1 t) + a_2 \exp(-k_2 t)$. The parameters k_1, k_2, a_1, a_2 and t are rate constants (k_1 and k_2), change amounts (a_1 and a_2) and reaction time (t) for two-stage (fast and slow) structural kinetics of the Pt nanoparticles.

The transient response profiles under 0.4 V_{RHE}→1.4 V_{RHE} and 1.4 V_{RHE}→0.4 V_{RHE} were successfully fitted with two and one exponential functions, respectively as shown by red curves in Figures 2 (A-E). The validity of the two component fittings is convinced from the comparison with the one component fittings in Figure S4. The determined rate constants for the electronic and structural changes and the change amounts are listed in Table S2. The rate constants thus obtained are not influenced by the Pt quantity and Pt utilization fraction in MEAs but affected by the working state of active Pt nanoparticles. This may be an advantage of the simultaneous QXAFS-XRD analysis of active catalyst itself over macroscopic electrochemical analysis. Figure 2 revealed that the Pt nanoparticles in the Pt/C cathode catalyst under the transient potential operation 0.4 V_{RHE}→1.4 V_{RHE} transform at two (fast and slow) successive steps with the rate constants k_1 and k_2. The rate constants (k_1 and k_2) for the changes in Pt charging (valence), CN(Pt-Pt) and CN(Pt-O) were 1.20 s^{-1} and 0.12 s^{-1}, 1.10 s^{-1} and 0.13 s^{-1}, and 1.60 s^{-1} and 0.15 s^{-1}, respectively. The rate constants (k_1 and k_2) for the changes in the integrated XRD (220) peak intensity and Pt metallic-phase size were 1.18 s^{-1} and 0.14 s^{-1} and 1.18 s^{-1} and 0.14 s^{-1}, respectively. Thus, it is indicated that the dynamic behavior of the Pt surface under 0.4 V_{RHE}→1.4 V_{RHE} is initiated with the Pt-O bond formation ($k_{1(Pt-O)}$=1.60 s^{-1}), followed by the Pt charging ($k_{1(valence)}$=1.20 s^{-1}) and Pt-Pt bond dissociation ($k_{1(Pt-Pt)}$=1.10 s^{-1}). The rate constants ($k_{1(XRD)}$=1.18 s^{-1}) for the Pt crystalline intensity and size changes (bulk change of Pt nanoparticles) were similar to those for the Pt charging and Pt-Pt bond dissociation. The surface Pt-O bond formation event was soon followed by the decreases in the Pt crystalline peak intensity and CN(Pt-Pt) (Pt-Pt bond dissociation) and the increase in the Pt charging, which suggests that the surface Pt-O bond formation induces the partial disordering (rearrangement) of the outermost Pt layer, resulting in an apparent half-layer decrease in the metallic-phase size at the saturated O layer from 2.78 nm to 2.64 nm as shown in Figure 2 (D) and (E) and in Figure 3.

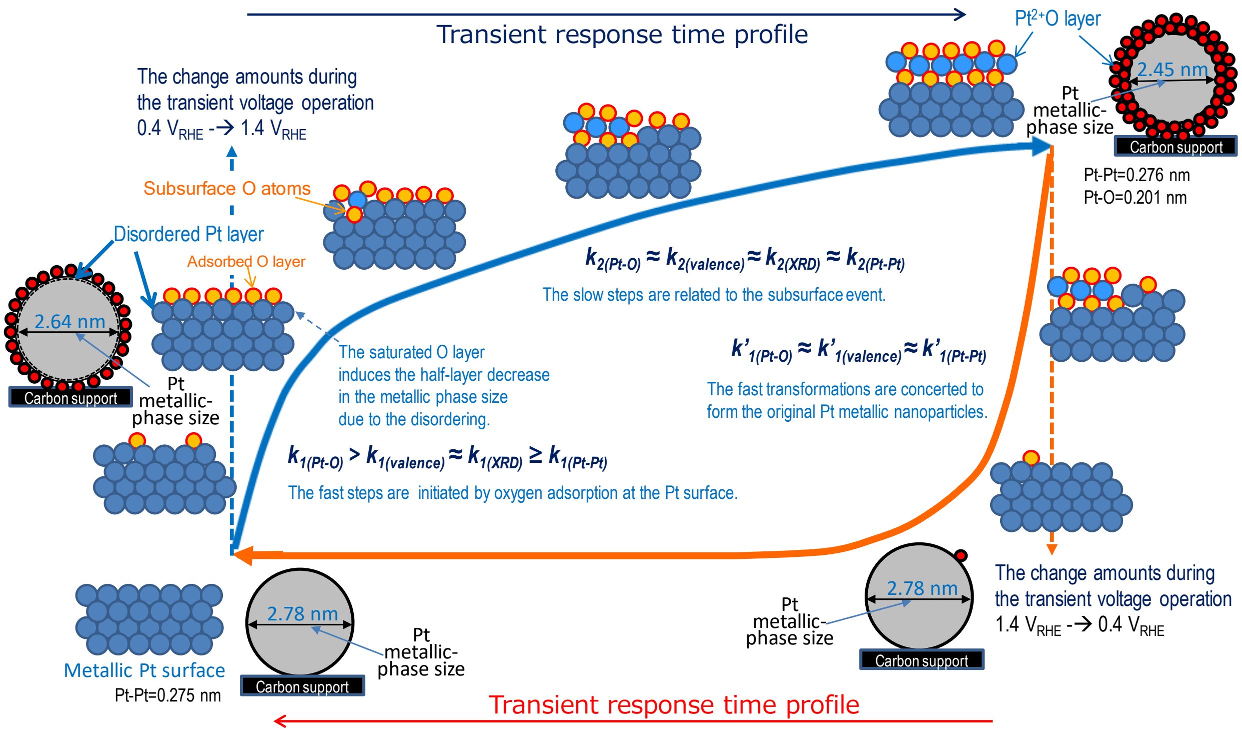

Figure 3. Reaction mechanism and structural kinetics for Pt surface events of an MEA Pt/C cathode catalyst under transient voltage cyclic operations 0.4 V_{RHE} -→ 1.4 V_{RHE} -→ 0.4 V_{RHE} under H_2(anode)-N_2(cathode). $k_{1(Pt-O)}$ & $k_{2(Pt-O)}$: Pt-O bond formation, $k_{1(valence)}$ & $k_{2(valence)}$: Pt charging, $k_{1(Pt-Pt)}$ & $k_{2(Pt-Pt)}$: Pt-Pt bond dissociation, $k_{1(XRD)}$ & $k_{2(XRD)}$: Pt metallic phase decrease, $k'_{1(Pt-O)}$) : Pt-O bond dissociation, $k'_{1(valence)}$: Pt discharging, $k'_{1(Pt-Pt)}$: Pt-Pt bond reformation, $k'_{1(XRD)}$: Pt metallic phase increase. If the 1.4 V_{RHE} -→ 0.4 V_{RHE} process was analyzed by two-component fitting, the rate constants $k'_{1(Pt-O)}$, $k'_{1(valence)}$, $k'_{1(XRD)}$ and $k'_{1(Pt-Pt)}$ were similar within error range.

The first fast surface event was followed by the second slow transformations of Pt-O bond formation, Pt charging, Pt-Pt bond dissociation and Pt nanoparticle size (metallic crystalline phase); $k_{2(Pt\text{-}O)}$=0.15 s^{-1}, $k_{2(valence)}$=0.12 s^{-1}, $k_{2(Pt\text{-}Pt)}$=0.13 s^{-1}, and $k_{2(XRD)}$=0.14 s^{-1} as shown in Figure 2 and Table S2. These rate constants are similar to each other within error ranges, which suggests that the second slow Pt-O bond formation, Pt charging, Pt-Pt bond dissociation and Pt metallic-phase size decrease occur concertedly to produce finally the tetragonal Pt^{2+}O layer (Pt-O=0.201 nm) at the Pt surface (Figure S2). The slow steps are related to the subsurface event (Figure 3).

Unlike the transient response transformations under 0.4 V$_{RHE}$→1.4 V$_{RHE}$, the transient response time profiles under 1.4 V$_{RHE}$→0.4 V$_{RHE}$ were fitted by one exponential function as shown in Figure 2; $k'_{1(valence)}$=1.04 s^{-1} for Pt discharging, $k'_{1(Pt\text{-}O)}$=0.86 s^{-1} for Pt-O bond dissociation, $k'_{1(Pt\text{-}Pt)}$=0.84 s^{-1} for Pt-Pt bond reformation, and $k'_{1(XRD)}$=1.32 s^{-1} for Pt metallic-phase size increase as shown in Figure 2 and Table S2. The $k'_{1(XRD)}$ was larger than the $k'_{1(Pt\text{-}O)}$ and $k'_{1(Pt\text{-}Pt)}$, but the metallic phase cannot increase unless the surface PtO layer is reduced to metallic Pt layer. There are larger error ranges in the XRD size analysis than in the QXANES analysis. We tentatively reanalyzed the QXAFS data in the 1.4 V$_{RHE}$→0.4 V$_{RHE}$ process by two component fittings, which also indicate the similar rate constants $k'_{1(XRD)}$, $k'_{1(valence)}$, $k'_{1(Pt\text{-}O)}$ and $k'_{1(Pt\text{-}Pt)}$ (Figure S6). Thus, the four chemical events, Pt discharging, Pt-O bond dissociation, Pt-Pt bond reformation and Pt metallic-phase increase, are regarded to proceed at nearly similar reaction rates under the present condition. The transformations under 1.4 V$_{RHE}$→0.4 V$_{RHE}$ are concerted to form the original Pt metallic nanoparticles. Nevertheless, further investigation on the convincing atomic-scale structural transformation for the 1.4 -> 0.4 V$_{RHE}$ process may be needed.

The averaged change amounts of the fast and slow parts in the time profiles of the Pt charging, Pt-O bond formation, Pt-Pt bond dissociation and Pt metallic-phase size under the transient potential operation 0.4 $\mathrm{V_{RHE}}$→1.4 $\mathrm{V_{RHE}}$ were 47% and 53%, respectively as shown in Figure 2 (inset). It suggests that the fast transformations proceed up to the nearly saturated oxygen coverage at the Pt surface, where CN(Pt-O) for surface Pt-O bonds at saturation is regarded to be 2.0, similar to the previous reports.[14] The Pt surface at 1.4 $\mathrm{V_{RHE}}$ is fully covered by the tetragonal PtO layer with CN(Pt-O)=4 (Figure S2). Thus, the transient response transformations of the Pt nanoparticles in MEA Pt/C under the voltage cyclic operations 0.4 $\mathrm{V_{RHE}}$→1.4 $\mathrm{V_{RHE}}$→0.4 $\mathrm{V_{RHE}}$, concluded by the simultaneous time-resolved QXAFS–XRD technique, are understood as the dynamic events concerned with the topmost Pt layer as illustrated in Figure 3 and Figure S4.

Conclusions

The first simultaneous operando time-resolved QXAFS–XRD approach to the Pt/C cathode catalyst in PEFC gained a new insight into the molecular-level reaction mechanism and dynamic transformation in the Pt surface layer under the transient potential operations by determining the rate constants $k_{1(Pt\text{-}O)}$ & $k_{2(Pt\text{-}O)}$ for Pt-O bond formation, $k_{1(valence)}$ & $k_{2(valence)}$ for Pt charging, $k_{1(Pt\text{-}Pt)}$ & $k_{2(Pt\text{-}Pt)}$ for Pt-Pt bond dissociation and $k_{1(XRD)}$ & $k_{2(XRD)}$ for Pt metallic-phase size decrease under 0.4 $\mathrm{V_{RHE}}$→1.4 $\mathrm{V_{RHE}}$, and $k'_{1(Pt\text{-}O))}$ for Pt-O bond dissociation, $k'_{1(valence)}$ for Pt discharging, $k'_{1(Pt\text{-}Pt)}$ for Pt-Pt bond reformation and $k'_{1(XRD)}$ for Pt metallic-phase size increase under1.4 $\mathrm{V_{RHE}}$→0.4 $\mathrm{V_{RHE}}$, which can aid the development of next-generation PEFCs with remarkable activity and durability. The application of the simultaneous time-resolved QXADFS-XRD technique to other PEFC cathode catalysts particularly under1.4 $\mathrm{V_{RHE}}$→0.4 $\mathrm{V_{RHE}}$ is in progress.

ASSOCIATED CONTENT

Supporting Information includes experimental procedures, analysis details, structural parameters determined by the EXAFS analysis, typical EXAFS Fourier transforms, structure models proposed by estimated coordination numbers for Pt-Pt and Pt-O bonds, Gaussian function fitting, and time profiles of the XRD (111) integrated peak intensity and the fittings.

AUTHOR INFORMATION

Corresponding Author

* Yasuhiro Iwasawa
Tel: +81-42-443-5921; E-mail: iwasawa@pc.uec.ac.jp

Author Contributions

The manuscript was written through contributions of all authors. All authors have given approval to the final version of the manuscript.

Conflict of Interest

The authors declare no competing financial interest.

ACKNOWLEDGMENT

This work was supported by the New Energy and Industrial Technology Development Organization (NEDO) of the Ministry of Economy, Trade, and Industry (METI), Japan. XAFS measurements were conducted at BL36XU beamline in SPring-8 (No. 2013A7802, 2013B7806, 2014A7801, 2014A7805, 2014B7801, 2014B7803, 2014B7805, 2015A7803, 2015A7840, 2015B7801, 2015B7803, 2015B7840, 2016A7801, 2016A7803, 2016A7840, 2016B7801, 2016B7803, 2016B7806, and 2016B7840).

References

(1) Bu, L.; Zhang, N.; Guo, S.; Zhang, X.; Li, J.; Yao, J.; Wu, T.; Lu, G.; Ma, J.-Y.; Su, D.; Huang, X. Biaxially strained PtPb/Pt core/shell nanoplate boosts oxygen reduction catalysis. *Science* **2016**, 354, 1410-1414.

(2) Wang, H.; Xu, S.; Tsai, C.; Li, Y.; Liu, C.; Zhao, J.; Liu, Y.; Yuan, H.; Abild-Pedersen, F.; Prinz, F. B.; Nørskov, J. K.; Cui, Y. Direct and continuous strain control of catalysts with

tunable battery electrode materials. *Science* **2016**, 354, 1031-1036.

(3) Stephens, I. E. L.; Bondarenko, A. S.; Grønbjerg, U.; Rossmeisl, J.; Chorkendorf, I. Understanding the electrocatalysis of oxygen reduction on platinum and its alloys. *Energy Environ. Sci.* **2012**, 5, 6744-6762.

(4) Debe, K. Electrocatalyst Approaches and Challenges for Automotive Fuel Cells. *Nature* **2012**, *486*, 43−51.

(5) Zhang, L.; Roling, L. T.; Wang, X.; Vara, M. V.; Chi, M.; Liu, J.; Choi, S.; Park, J.; Herron, J. A.; Xie, Z.; et al. Platinum-Based Nanocages with Subnanometer-Thick Walls and Well-Defined, Controllable Facets. *Science* **2015**, *349*, 412-416.

(6) Oezaslan, M.; Hasché, F.; Strasser, P. Pt-Based Core–Shell Catalyst Architectures for Oxygen Fuel Cell Electrodes. *J. Phys. Chem. Lett.* **2013**, *4*, 3273−3291.

(7) Nagasawa, K.; Takao, S.; Nagamatsu, S.; Samjeské, G.; Sekizawa, O.; Kaneko, T.; Higashi, K.; Yamamoto, T.; Uruga, T.; Iwasawa, Y. Surface-Regulated Nano-SnO_2/Pt_3Co/C Cathode Catalysts for Polymer Electrolyte Fuel Cells Fabricated by a Selective Electrochemical Sn Deposition Method. *J. Am. Chem. Soc.* **2015**, *137*, 12856−12864.

(8) Chen, C.; Kang, Y.; Huo, Z.; Zhu, Z.; Huang,W.; Huolin, W.; Xin, L.; Snyder, J. D.; Li, D.; Herron, J. A.; et al. Highly Crystalline Multimetallic Nanoframes with Three-Dimensional Electrocatalytic Surfaces. *Science* **2014**, *343*, 1339-1343.

(9) Borup, R.; Meyers, J.; Pivovar, B.; Kim, Y. S.; Mukundan, R.; Garland, N.; Myers, D.; Wilson, M.; Garzon, F.; Wood, D.; et al. Scientific Aspects of Polymer Electrolyte Fuel Cell Durability and Degradation. *Chem. Rev.* **2007**, *107*. 3904−3951.

(10) Stamenkovic, V. R.; Fowler, B.; Mun, B. S.; Wang, G.; Ross, P. N.; Lucas, C. A.; Marcovic, N. M. Improved Oxygen Reduction Activity on Pt_3Ni(111) via Increased Surface Site Availability. *Science* **2007**, *315*, 493−497.

(11) Tada, M.; Uruga, T.; Iwasawa, Y. Key Factors Affecting the Performance and Durability of Cathode Electrocatalysts in Polymer Electrolyte Fuel Cells Characterized by In Situ Real Time and Spatially Resolved XAFS Techniques. *Catal. Lett. (Silver Anniversary Special Issue)* **2015**, *145*, 58-70.

(12) Mukerjee, S.; Srinivasan, S.; Soriaga, M. P.; McBreen, J. Role of Structural and Electronic Properties of Pt and Pt Alloys on Electrocatalysis of Oxygen Reduction: An in Situ XANES and EXAFS Investigation. *J. Electrochem. Soc.* **1995**, *142*, 1409-1422.

(13) Adzic, R. R.; Wang, J. X.; Ocko, B. M.; McBreen, J. *EXAFS, XANES, SXS. Handbook of Fuel Cells*; Wiley: Online, 2010.

(14) Nagamatsu, S.; Takao, S.; Samjeské, G.; Nagasawa, K.; Sekizawa, O.: Kaneko, T.; Higashi, K.; Uruga, T.; Gayen, S.; Velaga, S.; et al. Structural and Electronic Transformations of Pt/C, Pd@Pt(1 ML)/C and Pd@Pt(2 ML)/C Cathode Catalysts in Polymer Electrolyte Fuel Cells during Potential-Step Operating Processes Characterized by in-Situ Time-resolved XAFS. *Surf. Sci.* **2016**, *648*, 100-113.

(15) Tada, M.; Murata, S.; Asaoka, T.; Hiroshima, K.; Okumura, K.; Tanida, H.; Uruga, T.; Nakanishi, H.; Matsumoto, S.; Inada, Y.; et al. In Situ Time-Resolved Dynamic Surface Events on the Pt/C Cathode in a Fuel Cell under Operando Conditions. *Angew. Chem. Int. Ed.* **2007**, *46*, 4310-4315.

(16) Ishiguro, N.; Kityakarn, S.; Sekizawa, O.; Uruga, T.; Sasabe, T.; Nagasawa, K.; Yokoyama, T.; Tada, M. Rate Enhancements in Structural Transformations of Pt–Co and Pt–Ni Bimetallic Cathode Catalysts in Polymer Electrolyte Fuel Cells Studied by in Situ Time-Resolved X-ray Absorption Fine Structure. *J. Phys. Chem. C* **2014**, *118*, 15874-15883.

(17) Ishiguro, N.; Saida, T.; Uruga, T.; Sekizawa, O.; Nagasawa, K.: Nitta, K.; Yamamoto, T.; Ohkoshi, S.; Yokoyama, T.; Tada, M. Structural Kinetics of a Pt/C Cathode Catalyst with Practical Catalyst Loading in an MEA for PEFC Operating Conditions Studied by in Situ Time-Resolved XAFS. *Phys. Chem. Chem. Phys.* **2013**, *15*, 18827-18834.

(18) Imai, H.; Izumi, K.; Matsumoto, M.; Kubo, Y.; Kato, K.; Imai, Y. In Situ and Real-Time Monitoring of Oxide Growth in a Few Monolayers at Surfaces of Platinum Nanoparticles in Aqueous Media. *J. Am. Chem. Soc.* **2009**, 131, 6293–6300.

(19) Nam, K.-W.; Bak, S.-M.; Hu, E.; Yu, X.; Zhou, Y.; Wang, X.; Wu, L.; Zhu, Y.; Chung, K.-Y.; Yang, X.-Q. Combining In Situ Synchrotron X-Ray Diffraction and Absorption Techniques with Transmission Electron Microscopy to Study the Origin of Thermal Instability in Overcharged Cathode Materials for Lithium-Ion Batteries. *Adv. Funct. Mater*. **2013**, 23, 1047–1063.

(20) Frenkel, A. I.; Wang, Q.; Marinkovic, N.; Chen, J. G.; Barrio, L.; Si, R.; Cámara, A. L.; Estrella, A. M.; Rodriguez, J. A.; Hanson, J. C. Combining X-ray Absorption and X-ray Diffraction Techniques for in Situ Studies of Chemical Transformations in Heterogeneous Catalysis: Advantages and Limitations. *J. Phys. Chem. C* **2011**, 115, 17884–17890.

TOC Graphic

Simultaneous Operando Time-Resolved XAFS–XRD Measurements of a Pt/C Cathode Catalyst in Polymer Electrolyte Fuel Cell under Transient Potential Operations

Oki Sekizawa,[†] *Tomoya Uruga,*[†,§] *Kotaro Higashi,*[†] *Takuma Kaneko,*[†] *Yusuke Yoshida,*[†] *Tomohiro Sakata,*[†] *and Yasuhiro Iwasawa*[†]*

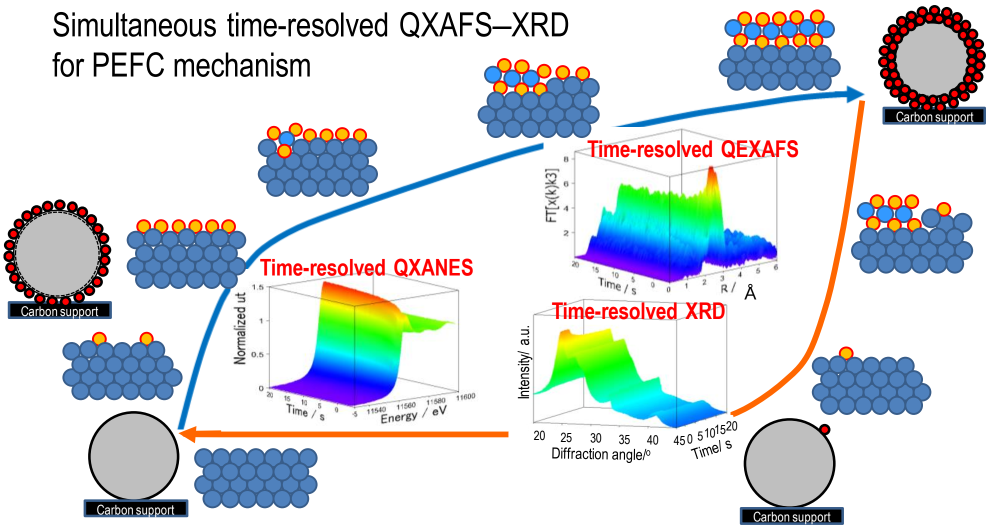

Supporting Information

Simultaneous Operando Time-Resolved XAFS–XRD Measurements of a Pt/C Cathode Catalyst in PEFC under Transient Potential Operations

Oki Sekizawa,[†] *Tomoya Uruga,*[†,§] *Kotaro Higashi,*[†] *Takuma Kaneko,*[†] *Yusuke Yoshida,*[†] *Tomohiro Sakata,*[†] *and Yasuhiro Iwasawa*[†]*

[†] Innovation Research Center for Fuel Cells, The University of Electro-Communications, Chofugaoka, Chofu, Tokyo 182-8585, Japan

[§] Japan Synchrotron Radiation Research Institute, SPring-8, Sayo, Hyogo 679-5198, Japan

Combination of XAFS and XRD for *in situ* characterization of catalysts and nanomaterials has been reported by several groups. Pt/C at rotating disk electrode in 0.5 M H_2SO_4 was characterized by XAFS and XRD separately at the time resolution of 0.9 s and 0.5 s at different beamlines (H. Imai et al. *J. Am. Chem. Soc.* 2009, *131*, 6293–6300). Cu particle growth by reduction of $CuFe_2O_4$ and CuO/CeO_2 was measured by XAFS and XRD separately at the time resolution of 0.5-15 s and 30 s, respectively (A. I. Frenkel et al. *J. Phys. Chem. C* 2011, 115, 17884–17890). Thermal stability of $Li_xNi_{0.8}Co_{0.15}Al_{0.05}O_2$ and $Li_xNi_{1/3}Co_{1/3}Mn_{1/3}O_2$ cathode materials at high temperature was studied by XRD and XAFS separately at the time resolution of 2.6 min and ~10 min, respectively (K.-W. Nam et al. *Adv. Funct. Mater.* 2013, *23*, 1047–1063). Water gas shift reaction on CuO_x/CeO_2 was monitored by XAFS (no time resolution) and XRD (min order acquisition time) separately (X. Wang et al. *Top. Catal.* 2008, 49, 81–88). IrNi@Ir/C catalyst in a flow cell was measured by XRD (2.6 min acquisition time) and XAFS (no time resolution) separately (K. Sasaki et al. *J. Phys. Chem. C* 2011, 115, 9894–9902). In contrast to these XAFS-XRD measurements separately at different beamlines, H_2 reduction process of Cu/SiO_2 was observed at the same beamline by XAFS and XRD at the time resolution of 120 s and 90 s, respectively though the study was not a simultaneous measurement approach (B.S. Clausen et al. *Catal. Lett.* 1993, 20, 23-36). Here we report the first example of simultaneous *operando* time-resolved QXAFS–XRD measurements at each acquisition time of 20 ms to evidence the dynamic structural and electronic behavior of an MEA Pt/C cathode catalyst under the transient voltage cyclic operations 0.4 V →1.4 V →0.4 V (vs RHE).

Experimental: detailed description

MEA cathode catalysts and electrochemical measurements. A cathode catalyst was Pt/C (Pt 46.1 wt%, TEC10E50E, Tanaka Kikinzoku Kogyo), and Ru/C (Ru 30 wt%, TECRu(ONLY)E50, Tanaka Kikinzoku Kogyo) was used as an anode catalyst to avoid interference against XAFS measurements of the Pt/C cathode. The MEA used in this study, which constitutes an anode layer, a Nafion® NR-212 membrane (Sigma-10 Aldrich) and a cathode layer, was provided by Eiwa Co. Ltd., Japan. The size of the MEA was 3.0 × 3.3 cm, and catalyst loadings at the cathode and anode were 0.6 mg-Pt/Ru cm^{-2}. The prepared MEAs were sandwiched in a home-made XAFS cell using Viton® gaskets of 0.15 mm thickness, gas diffusion layers (GDL:TGP-H-060 (10wt% PTFE treatment)) and separator-plates (bipolar plates) with serpentine-shape type flow channels for both anode and cathode sides. The average particle size in the fresh (activated) Pt/C catalyst in MEA was estimated to be 2.6 ± 0.9 nm by the analysis of TEM images.

The cathode was connected as working electrode and the anode (hydrogen-fed) served as combined counter and reference electrode. All potentials are referred to this pseudo hydrogen reference electrode (RHE). The gas flows of H_2 (99.99999%; 100 sccm) for anode and N_2 (99.99995%; 600 sccm) or air (99.99995%; 900 sccm) for cathode were regulated by mass-flow controllers and were bubbled through humidifiers at 351 K. The humidified gases were supplied to the *in situ* XAFS cell heated at 353 K, resulting in ~ 93% relative humidity (RH). The MEAs in the XAFS cell were conditioned by 150 aging cycles with a sequence of step-wise galvanostatic current steps every 6 s from open circuit voltage (OCV) to a potential near 0.3 V_{RHE} in H_2 (anode) and air (cathode) operating atmospheres. Cyclic voltammograms (CVs) and I-V loads under were measured after the aging treatment. The CV measurements in *in situ* PEFC conditions were conducted between 0.05 and 0.9 V_{RHE} at 20 mV s^{-1} in H_2 (anode) and N_2 (cathode) operating atmospheres. The cell voltage was controlled using a potentiostat-galvanostat (Autolab PGSTAT302N, Metrohm, Netherlands) and Current amplifier (Autolab BOOSTER20A, Metrohm).

In situ time-resolved XAFS and XRD measurements. The series of *in situ* time-resolved Pt L_{III}-edge XAFS spectra and *in situ* time-resolved XRD patterns for Pt/C in MEA under transient potential operations (anode: H_2; cathode: N_2; 353 K; ~93% relative humidity) were measured at BL36XU station in SPring-8, where the incident X-rays were irradiated to Pt/C cathode catalysts in an in situ PEFC cell at an angle of 10^o to the MEA plane. The experimental setup for *in situ* time-resolved XAFS and XRD measurements, while measuring the current/charge of PEFC during the potential operating processes, is shown in Figure 1. The quick-XAFS (QXAFS) spectra were measured in a transmission mode by using a Si(111) channel-cut monochromator on a high-speed galvano scanner, and using high-speed ion chambers (S1196D1, OKEN). The PEFC cell was placed between I_0 ion chamber (Ar 15%/N_2 85%) and I_1 ion chamber (Ar 50%/N_2 50%), and Pt foil was placed between I_1 ion chamber and I_2 ion chamber (Ar 50%/N_2 50%) for energy calibration.

The cell voltage was controlled using a potentiostat-galvanostat (Autolab PGSTAT302N, Metrohm, Netherlands) and Current amplifier (Autolab BOOSTER20A, Metrohm). The cell voltage was changed from the open-circuit voltage (OCV) to 0.4 V_{RHE}, where the voltage was kept for 300 s, followed by the rapid voltage jump from 0.4 V_{RHE} to1.4 V_{RHE} (at time=zero for the transient voltage up process), and this voltage was kept for 300 s, and then reversely, the cell voltage was jumped rapidly from 1.4 V_{RHE} to 0.4 V_{RHE} (at time=zero for the transient voltage down process). The transient responses of the MEA cathode catalysts against the voltage cycling operations were measured by time-resolved QXAFS at a time resolution of 20 ms for 30 s from 10 s before each voltage jump.

In situ time-resolved XRD measurements were conducted every 20 ms (acquisition time: 17 ms, read out time: 3 ms) at an incidence X-ray energy of 12,638 eV in the 2θ range of 20 – 45° using a high-speed 2D detector ((PILATUS 300K-W, DECTRIS), while measuring the current/charge of PEFC during the potential operating processes. The transient responses of the MEA cathode catalysts against the voltage cycling operations for 30 s from 10 s before each voltage jump were also measured by the *in situ* time-resolved XRD technique using a 24bit ADC (analog digital converter; PXI-5922) for PILATUS signals and a TTL trigger of a potentio-galvanostat for time-resolved XRD measurement.

In situ time-resolved XAFS and XRD analyses. QXANES and QEXAFS spectra were analyzed in the similar way to the previous reports,[11,14,15(text)] using the Larch code (v0.9.20a) containing the IFEFFIT Package (Athena and Artemis).[ref.1] The white line peaks of normalized QXANES spectra were analyzed by curve fitting with a Lorentzian function and an arctangent function. Background subtraction in QEXAFS analysis was performed using Autobk program.[ref.2] The extracted k^3-weighted Pt L_{III}-edge EXAFS oscillations were Fourier transformed into R-space over k = 30–130 nm^{-1}, and the curve fittings were performed in the R-space (0.12–0.31 nm). The fitting parameters for each shell were the coordination number (CN), interatomic distance (R), Debye–Waller factor (σ^2), and correction-of-edge energy (ΔE_0). The phase shifts and backscattering amplitude for each shell were calculated with FEFF8.5-Lite code using structural parameters obtained from the crystal structures of Pt and PtO_2.[ref.3] Self-consistent field potentials were added to the FEFF calculations for the reliable determination of the Fermi level. The amplitude reduction factor (S_0^2) for Pt-Pt bonds in this study was estimated to be 0.916 by analyzing Pt foil.

For the time-resolved XRD analysis we measured XRD patterns for a brank cell with a Nafion membrane and without catalyst layers and removed background signals by correcting the XRD data with a non-linear scale factor. XRD (220) diffraction peak was fitted by the pseudo-Voigt function and Pt particle sizes in MEA Pt/C cathode catalysts were calculated by the Scherrer equation.

[Ref.1] Newville, M.; Ravel, B.; Haskel, D.; Rehr, J. J.; Stern, E. A.; Yacoby, Y. Analysis of Multiple-Scattering XAFS Data Using Theoretical Standards. *Phys. B* **1995**, *208–209*, 154-156.

[Ref.2] Ravel, B.; Newville, M. ATHENA, ARTEMIS, HEPHAESTUS: Data Analysis for X-ray Absorption Spectroscopy Using IFEFFIT. *J. Synchrotron Rad.* **2005**, *12*, 537-541.

Ref.3 Rehr J. J.; Albers, R. C. Theoretical Approaches to X-ray Absorption Fine Structure. *Rev. Mod. Phys.* **2000**, *72*, 621-654.

Rate constants. The white line peak height of the Pt L_{III}-edge QXANES, the coordination number (CN) of Pt-Pt and Pt-O, and the current/charge variation of PEFC MEA recorded on the electrochemical P/G stat were plotted against time in the transient response processes under the potential jump of 0.4 V_{RHE} →1.4 V_{RHE} and 1.4 V_{RHE} →0.4 V_{RHE}. The rate constants for six elementary reaction processes at cathode Pt catalyst surfaces determined from the time change in the above parameters were estimated by QXAFS data fitting using a linear combination of two exponential functions for the potential-gain jump (0.4 V_{RHE} → 1.4 V_{RHE}) and using an exponential function for the potential-down jump (1.4 V_{RHE} → 0.4 V_{RHE}), taking into account the error weighting given by the inverse of the error.[14 (text), Ref.4] The rate constants for the XRD change processes were also determined by fitting the time changes in the XRD integrated peak intensity and Pt particle size by one or two exponential functions. The data fittings with one or two exponential functions for the QXAFS and XRD analysis data were performed for the period of 0–20 s after the potential was jumped. It is to be noted that the analysis of QXAFS and XRD data by exponential functions to determine the first-order rate constants is independent of Pt quantity and Pt utilization in MEAs and reflects the dynamic changes of the Pt valence and local coordination structure and the long-period ordered structure in the transient response processes against the potential operations.

Ref.4 Kaneko, T.; Samjeské, G.; Nagamatsu, S.; Higashi, K.; Sekizawa, O.; Takao, S.; Yamamoto, T.; Zhao, X.; Sakata, T.; Uruga, T.; Iwasawa, Y. *J. Phys. Chem. C*, **2016**, 120, 24250–24264.

XRD peak integrated intensity and Pt metallic-phase size. Integrated intensity was calculated by Gaussian function fitting. Pt metallic-phase size was calculated by the Scherrer equation (K=1) using integral width from the Gaussian function fitting.

Gaussian function (integral width)

$$f(\theta) = \frac{A\sqrt{\pi}}{\beta} exp\left\{-\pi\left[\frac{2(\theta-\theta_0)}{\beta}\right]^2\right\}$$

A: integrated intensity
β: integral width
θ_0: peak position

Scherrer equation

$$\mathrm{D} = \frac{K\lambda}{\beta\cos\theta}$$

D: particle sizes
K: shape factor
λ: wavelength
β: line broadening
θ: Bragg angle

Surface structures of Pt nanoparticles in MEA Pt/C at 0.4 V_{RHE} and 1.4 V_{RHE}

For the cathode catalysts at 0.4 V_{RHE} only Pt-Pt bonds at 0.275 ±0.001 nm were observed, indicating the metallic state of Pt nanoparticles on carbon. The coordination numbers (CN) of Pt-Pt were 9.6 ± 0.8. The Pt nanoparticles with 2.6 (± 0.9) nm dimension are regarded to constitute approximately 5 Pt layers (the fifth, fourth, third, second, and first layers and a central atom), assuming sphere structures with the fcc arrangement (d_{111} (interplanar spacing) ~0.23 nm), and hence the CN(Pt-Pt) is estimated to be 10.6 by eq.(S1),

$$\text{CN(Pt-Pt)}=(12*(1^2+2^2+3^2+4^2)+9*5^2)/\ (1^2+2^2+3^2+4^2+5^2)=10.6 \qquad \text{eq.(S1)},$$

where 12 is the CN of Pt atoms in fcc Pt bulk(1st-4th Pt layer) and 9 is the CN of Pt atoms at the outermost surface (5th Pt layer).[14(text)] The observed CN(Pt-Pt) value is compatible with 10.6, taking into account the experimental error ranges in both XAFS and TEM. Alternatively, a part of the surface of the Pt nanoparticles supported on carbon may be distorted, resulting in a decrease of the CN(Pt-Pt). At 1.4 V_{RHE}, the Fourier transform of the QEXAFS data was fitted with two shells of Pt-Pt at 0.276 ±0.001 nm and Pt-O at 0.201 ±0.002 nm (Table S1), indicating the oxidation of the Pt catalyst surface as reported previously for Pt/KB, Pt/AB, Pt/MWCNT, Pt_3Co/KB, Pt_3Ni/KB, SnO_2/Pt/KB and SnO_2/Pt_3Co/KB.[7,11,14-17(text)] The CN(Pt-Pt) and CN(Pt-O) were determined to be 5.3 ±1.0 and 2.2 ± 0.5, respectively (Table S1). From the CN(Pt-Pt) and CN(Pt-O) we estimated the surface structures of Pt nanoparticles on carbon at 1.4 V_{RHE} in a similar way to that described in our previous study.[11,14,15(text)] The CN(Pt-Pt) decreased drastically from 9.6 to 5.3, which indicates the existence of both surface oxygen and subsurface oxygen, forming a surface $Pt^{2+}O$ layer. The observed Pt-O bond distance of 0.201 ±0.002 nm (Table S1) is similar to 0.200 nm for tetragonal PtO phase. By assuming a full coverage of tetragonal PtO phase at the Pt nanoparticle surface (Figure S2), the CN(Pt-Pt) and CN(Pt-O) values are estimated to be 5.7 and 2.4, respectively by eq.(S2) and eq.(S3).

$$\text{CN(Pt-Pt)}=12*(1^2+2^2+3^2)/(1^2+2^2+3^2+4^2+5^2)+9*4^2/(1^2+2^2+3^2+4^2+5^2)=5.7 \qquad \text{eq.(S2)}$$

$$\text{CN(Pt-O)}=(5^2*4+4^2*2)/(1^2+2^2+3^2+4^2+5^2)=2.4 \qquad \text{eq.(S3)}$$

These values well reproduce the observed CN values for Pt/C. The potential dependent surface structures at 0.4 V_{RHE} and 1.4 V_{RHE} are illustrated in Figure S2 (a) and (b), respectively.

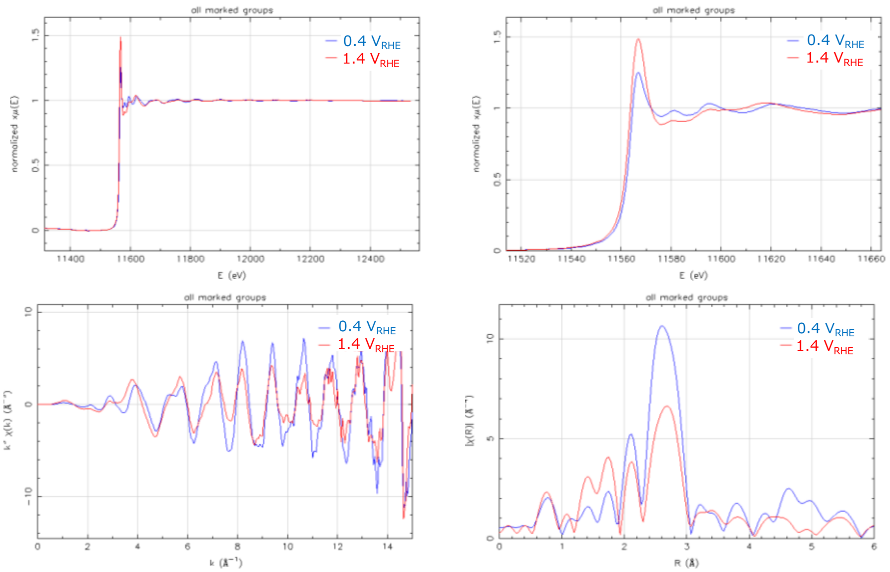

Figure S1. The typical XAFS spectra measured at 20 ms acquisition time for Pt/C in PEFC, their oscillations and Fourier transforms at 0.4 V_{RHE} and 1.4 V_{RHE} during voltage jump 0.4 V_{RHE} →1.4 V_{RHE}.

Table S1. Structural parameters determined by the curve-fitting analysis of *in situ* Pt L_{III}-edge QEXAFS Fourier transforms for the MEA Pt/C cathode under H_2(anode)-N_2(cathode).

Voltage	Shell	CN	R / nm	ΔE_0/eV	σ^2 / 10^{-5} nm^2	R-factor
0.4 V_{RHE}	Pt-Pt	9.6±0.8	0.275±0.001	4.4±0.5	7.2±0.2	0.2 %
1.4 V_{RHE}	Pt-Pt	5.3±1.0	0.276± 0.001	5.0±2.0	7.0±0.8	0.9 %
	Pt-O	2.2± 0.5	0.201± 0.002	6.0±3.0	7.0±2.0	

$S_0^2 = 0.916$, Δk = 30-130 nm^{-1}, ΔR = 0.12-0.31 nm.

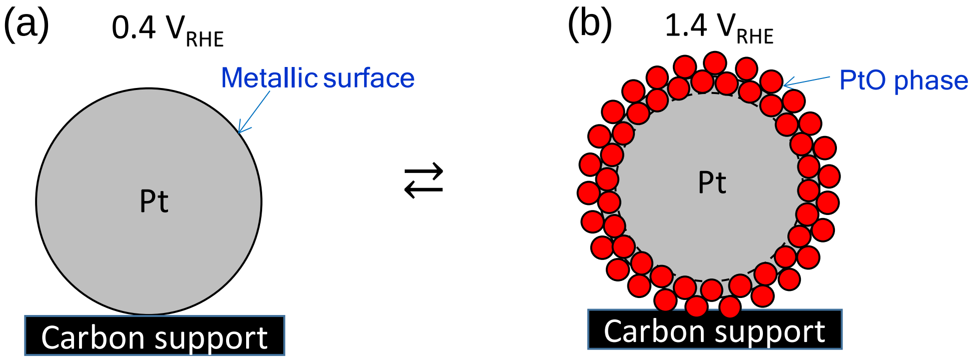

Figure S2. Potential-dependent surface structures of Pt nanoparticles in Pt/C cathode at 0.4 V$_{RHE}$ (a) and 1.4 V$_{RHE}$ (b).

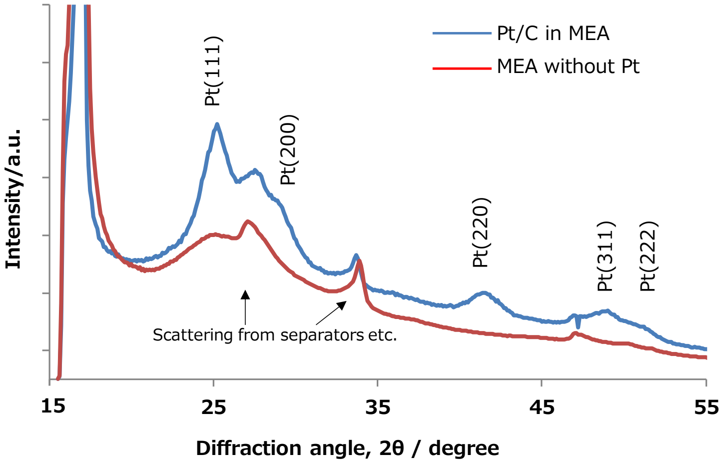

Figure S3. A typical XRD pattern for the Pt/C cathode catalyst in MEA (acquisition time: 20 ms). Cathode: Pt 46.1 wt%, 0.62 mg$_{Pt}$ cm-2, Pt/C (TEC10E50E, Tanaka Kikinzoku Kogyo), Anode: Ru 30 wt%, Ru/C (TECRu(ONLY)E50, Tanaka Kikinzoku Kogyo)

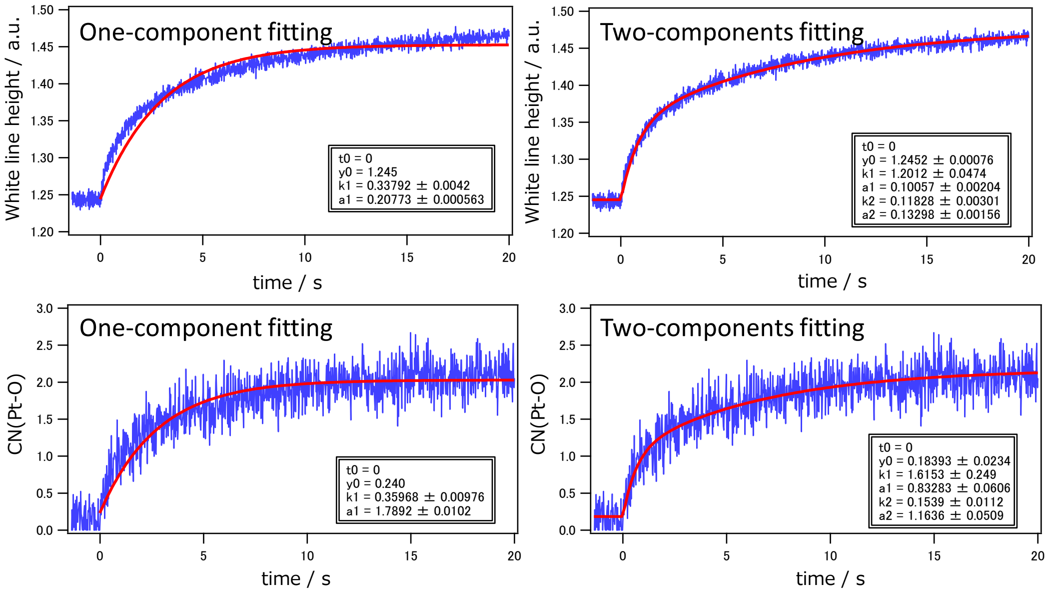

Figure S4. Transient response curves (blue) and one or two components fittings (red) of the white line peak height and CN(Pt-O) of the MEA Pt/C catalyst in the potential operations (0.4 V_{RHE}→1.4 V_{RHE}) under H_2(anode)–N_2(cathode); Cell temp.: 353 K; Relative humidity: ~93%. Acquisition time: 20 ms.

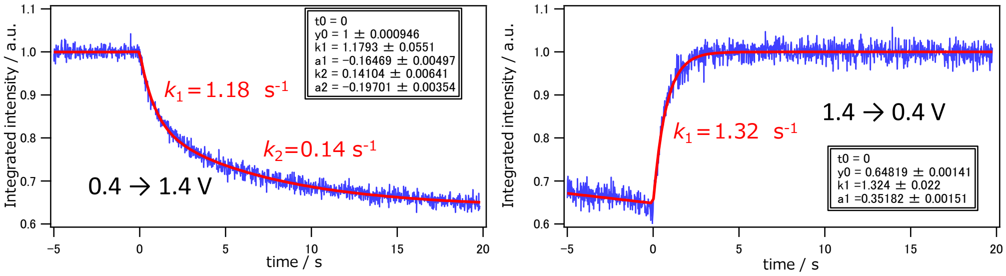

Figure S5. Transient response curves of the integrated (111) peak intensity of the MEA Pt/C catalyst in the potential operations (0.4 V_{RHE}→1.4 V_{RHE}→0.4 V_{RHE}) under H_2(anode)–N_2(cathode); Cell temp.: 353 K; Relative humidity: ~93%. Time resolution: 20 ms.

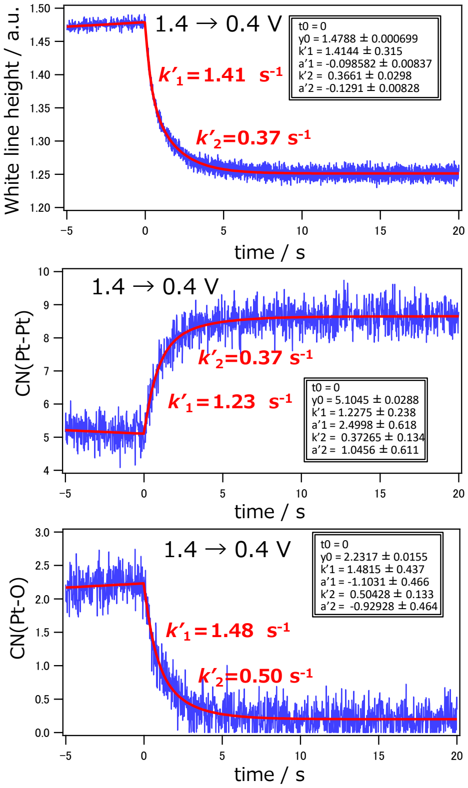

Figure S6. Transient response curves of the white line peak height, CN(Pt-Pt) and CN(Pt-O) of the MEA Pt/C catalyst in the potential operations (1.4 V_{RHE}→0.4 V_{RHE}) under H_2(anode)–N_2(cathode); Cell temp.: 353 K; Relative humidity: ~93%. Time resolution: 20 ms.

We expected the rate constants k'_{1XRD} and $k'_{1Pt\text{-}Pt}$ estimated by XRD and EXAFS are similar to each other, but the rate constant 1.32 s^{-1} for the k'_{1XRD} was larger than the rate constant 0.84 s^{-1} for the $k'_{1Pt\text{-}Pt}$ though the difference is not so much. At the moment we think that the difference is not significant because the difference may derive from the larger error ranges in the XRD size analysis than in the QXANES analysis and also from error ranges in the one-component fittings for the XAFS data in the 1.4 -> 0.4 V_{RHE} process. We carefully re-analyzed the XAFS data by two-component fittings similar to the case of the 0.4 -> 1.4 V_{RHE} process. The rate constant $k'_{1Pt\text{-}Pt}$ determined by the two component fitting was 1.23±0.24 s^{-1}, which is similar to 1.32 s^{-1} for the rate constant k'_{1XRD}, and the rate constants for $k'_{1Pt\text{-}O}$ and $k'_{1valence}$ were 1.48±0.44 s^{-1} and 1.41±0.32 s^{-1}, respectively. Thus, the rate constants $k'_{1(Pt\text{-}O)}$, $k'_{1(valence)}$, $k'_{1(XRD)}$ and $k'_{1(Pt\text{-}Pt)}$ were similar within error range. The two-component fittings were shown in Figure S6. However, the difference in fitting quality between the one- and two-components fittings is small. Further investigation on the convincing atomic-scale structural transformation for the 1.4 -> 0.4 V_{RHE} process may be needed. Nevertheless, the simultaneous time-resolved

XAFS-XRD approach provides deeper understanding of Pt/C cathode catalysts inside MEA in PEFC under potential operating conditions.

Table S2. Rate constants and change amounts of the structural changes in the MEA Pt/C cathode catalyst under the transient potential operations (0.4 V_{RHE}→1.4 V_{RHE} and 1.4 V_{RHE}→0.4 V_{RHE})

0.4→1.4 V_{RHE}	k_1 / s^{-1}	a_1 / a.u.	k_2 / s^{-1}	a_2 / a.u.
111 int	1.18±0.05	-0.16±0.00	0.14±0.01	-0.20±0.00
220 int	1.18 (fixed)	-0.12±0.00	0.14 (fixed)	-0.14±0.00
220 size	1.18 (fixed)	-0.14±0.00	0.14 (fixed)	-0.14±0.01
White line	1.20±0.05	0.10±0.00	0.12±0.00	0.13±0.00
CN_{Pt-Pt}	1.10±0.10	-2.1±0.1	0.13±0.01	-1.6±0.1
CN_{Pt-O}	1.60±0.20	0.83± 0.06	0.15±0.01	1.16±0.05
1.4→0.4 V_{RHE}	k'_1 / s^{-1}	a_1 / a.u.		
111 int	1.32±0.02	0.35±0.00		
220 int	1.32 (fixed)	0.21±0.00		
220 size	1.32 (fixed)	0.33±0.01		
White line	1.04±0.01	-0.23±0.00		
CN_{Pt-Pt}	0.84±0.02	3.49±0.01		
CN_{Pt-O}	0.86±0.02	-2.01±0.01		

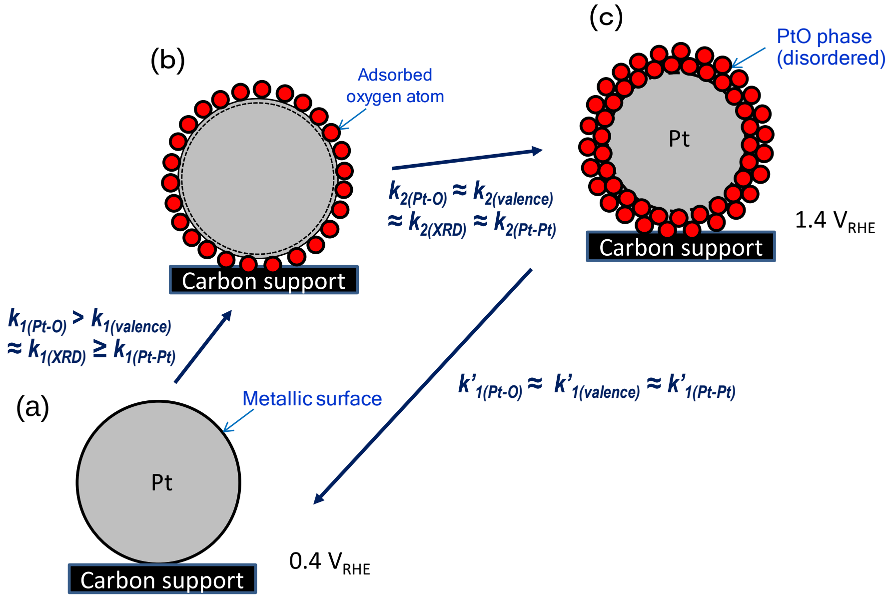

Figure S4 . Reaction mechanism and structural kinetics for Pt surface events of an MEA Pt/C cathode catalyst under transient voltage cyclic operations 0.4 V_{RHE} -→ 1.4 V_{RHE} -→ 0.4 V_{RHE} under H_2(anode)-N_2(cathode). $k_{1(Pt-O)}$ & $k_{2(Pt-O)}$: Pt-O bond formation, $k_{1(valence)}$ & $k_{2(valence)}$: Pt charging, $k_{1(Pt-Pt)}$ & $k_{2(Pt-Pt)}$: Pt-Pt bond dissociation, $k_{1(XRD)}$ & $k_{2(XRD)}$: Pt metallic phase decrease, $k'_{1(Pt-O))}$: Pt-O bond dissociation, $k'_{1(valence)}$: Pt discharging, $k'_{1(Pt-Pt)}$: Pt-Pt bond reformation, $k'_{1(XRD)}$: Pt metallic phase increase.